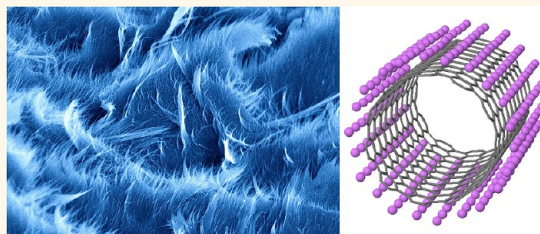# Influence of Electronic Type Purity on the Lithiation of Single-Walled Carbon Nanotubes

Laila Jaber-Ansari,[†] Hakim Iddir,[‡] Larry A. Curtiss,[‡] and Mark C. Hersam[†,§,*]

[†]Department of Materials Science and Engineering, Northwestern University, Evanston, Illinois 60208, United States, [‡]Materials Science Division, Argonne National Laboratory, Argonne, Illinois 60439, United States, and [§]Department of Chemistry, Northwestern University, Evanston, Illinois 60208, United States

ABSTRACT Single-walled carbon nanotubes (SWCNTs) have emerged as one of the leading additives for high-capacity nanocomposite lithium ion battery electrodes due to their ability to improve electrode conductivity, current collection efficiency, and charge/discharge rate for high power applications. However, since as-grown SWCNTs possess a distribution of physical and electronic structures, it is of high interest to determine which subpopulations of SWCNTs possess the highest lithiation capacity and to develop processing methods that can enhance the lithiation capacity of underperforming SWCNT species. Toward this end, SWCNT electronic type purity is controlled *via* density gradient ultracentrifugation, enabling a systematic study of the lithiation of SWCNTs as a function of metal *versus* semiconducting content. Experimentally, vacuum-filtered freestanding films of metallic SWCNTs are found to accommodate lithium with an order of magnitude higher capacity than their semiconducting counterparts, which is consistent with *ab initio* molecular dynamics and density functional theory calculations in the limit of isolated SWCNTs. In contrast, SWCNT film densification leads to the enhancement of the lithiation capacity of semiconducting SWCNTs to levels comparable to metallic SWCNTs, which is corroborated by theoretical calculations that show increased lithiation of semiconducting SWCNTs in the limit of small SWCNT—SWCNT spacing. Overall, these results will inform ongoing efforts to utilize SWCNTs as conductive additives in nanocomposite lithium ion battery electrodes.

KEYWORDS: density gradient ultracentrifugation · semiconducting · metallic · lithium ion battery · density functional theory · *ab initio* molecular dynamics

Carbon nanotubes (CNTs) have been studied extensively for their application in lithium ion batteries due to their favorable physical and chemical properties.[1−16] For example, their nanometer-scale size allows for short lithium diffusion times, making them promising candidates for high-power lithium ion batteries.[13] Furthermore, their high aspect ratio and electrical conductivity, combined with high mechanical strength and resilience, enable the formation of robust CNT networks that can support other materials such as silicon,[1,17,18] metal oxides,[2,6,10,19−21] and lithium metal oxides[4,7,22] in nanocomposite anodes and cathodes. In bulk form, these materials experience large volume changes during lithiation and delithiation that result in mechanical fracture, thus losing electrical contact with the current collector and ultimately leading to capacity loss of the battery.[23,24] In contrast, the presence of a CNT network in a nanocomposite electrode increases battery life and safety by mechanically reinforcing the electrode and preserving electrical contact with the current collector. CNTs have proven to be so advantageous that these networks have replaced metallic current collectors in recent studies, leading to improvements in adhesion of the active electrode material, enhanced mechanical durability, and lower contact resistance in comparison with metal current collectors.[25,26]

Despite the increasing application of CNTs in lithium ion battery electrodes and the well-known structural and electronic polydispersity of as-grown single-walled carbon nanotubes (SWCNTs),[27,28] the effects of SWCNT structure and electronic properties on lithiation have not been reported. Furthermore, experimental studies and

theoretical calculations performed on the interaction of lithium with SWCNTs have primarily considered either individual SWCNTs[29,30] or bundles of small-diameter (<1.2 nm) SWCNTs,[31,32] despite the improved SWCNT—SWCNT contact and thus higher electrical conductivity of large-diameter (>1.2 nm) SWCNTs and bundles.[33] In this paper, we address these issues by performing an experimental and theoretical analysis of the lithiation of large-diameter SWCNTs that have been sorted by electronic type (i.e., metallic versus semiconducting) with density gradient ultra-centrifugation (DGU). Furthermore, we control the SWCNT—SWCNT spacing (i.e., degree of bundling) by varying the densification of SWCNT thin films. This study reveals that as-produced vacuum-filtered metallic SWCNT thin films possess an order of magnitude higher lithiation capacity than semiconducting SWCNTs, as predicted by theoretical calculations in the limit of noninteracting (i.e., unbundled) SWCNTs. On the other hand, densification of the SWCNT thin films (i.e., bundled SWCNTs) increases the lithiation capacity of the previously underperforming semiconducting SWCNTs to a level that is comparable to metallic SWCNTs, again in agreement with theoretical calculations. In this manner, this work provides fundamental understanding and guidance to researchers interested in optimizing the performance of SWCNT-based lithium ion battery electrodes.

EXPERIMENTAL RESULTS

As-grown SWCNTs are approximately 67% semiconducting and 33% metallic. Although a few growth techniques exist that result in SWCNTs enriched in specific chiralities or electronic type,[34,35] the resulting purities are typically insufficient for high-performance applications, thus necessitating postgrowth sorting techniques.[36−38] Density gradient ultracentrifugation[33,37,39−41] is an appropriate choice for sorting SWCNTs for lithium ion battery studies because it can be applied to SWCNTs with different diameters, yields electronic type purities in excess of 99% for both metallic and semiconducting SWCNTs, and can be scaled up to sufficiently large quantities to enable the fabrication of freestanding battery electrodes.

In DGU, SWCNTs are dispersed in deionized water using ionic surfactants and then injected into an aqueous density gradient. The buoyant density of the surfactant-dispersed SWCNTs depends on the SWCNT diameter in addition to the amount and type of surfactant surrounding the SWCNT. Consequently, surfactant selection allows the relationship between SWCNT structure/properties and buoyant density to be tuned. Upon ultracentrifugation, the surfactant-dispersed SWCNTs sediment to their respective isopycnic points (i.e., the point where the SWCNT buoyant density matches the density gradient medium), resulting in the formation of distinct SWCNT bands with uniform diameter and/or electronic type.[33,41] These bands are then fractionated, yielding a monodisperse SWCNT population that can be used to fabricate freestanding films via vacuum filtration or related film formation techniques.

DGU with the ionic surfactants sodium cholate (SC) and sodium dodecyl sulfate (SDS) was employed to sort the large-diameter (>1.2 nm) arc discharge SWCNTs in this work. Following DGU, fractions of metallic or semiconducting SWCNTs were isolated and characterized by optical absorbance spectroscopy (Figure 1a). The absorbance peaks for metallic (M11 and M22) and semiconducting (S22 and S33) SWCNTs are indicated. The relative area under the absorbance peaks for the metallic and semiconducting transitions allows the electronic purity to be estimated.[33] The sorted aqueous SWCNT dispersion was then vacuum-filtered to a freestanding SWCNT film as shown in Figure 1b. The film was rinsed several times with deionized water to remove the majority of the surfactants. Nevertheless, surfactants cannot be rinsed off completely, leading to residual surfactant at a level less than ~15 wt %.[42]
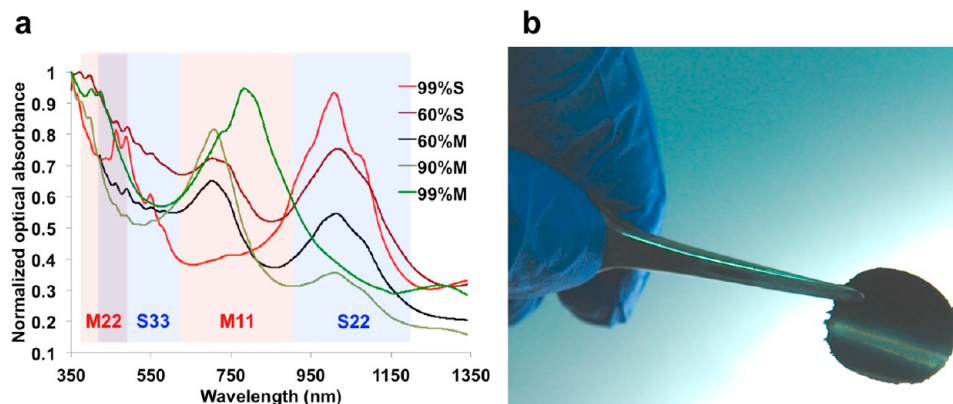
Figure 1. (a) Optical absorbance spectra of sorted SWCNT solutions, showing optical transitions for different metallic and semiconducting purities. Wavelengths associated with second- and third-order semiconducting transitions (shaded blue) and first- and second-order metallic transitions (shaded red) are labeled S22, S33, M11, and M22, respectively. The electronic type purity was estimated from the area under the metallic and semiconducting peaks. (b) Photograph of a freestanding SWCNT film that was fabricated by vacuum filtration and then peeled off the filter paper.
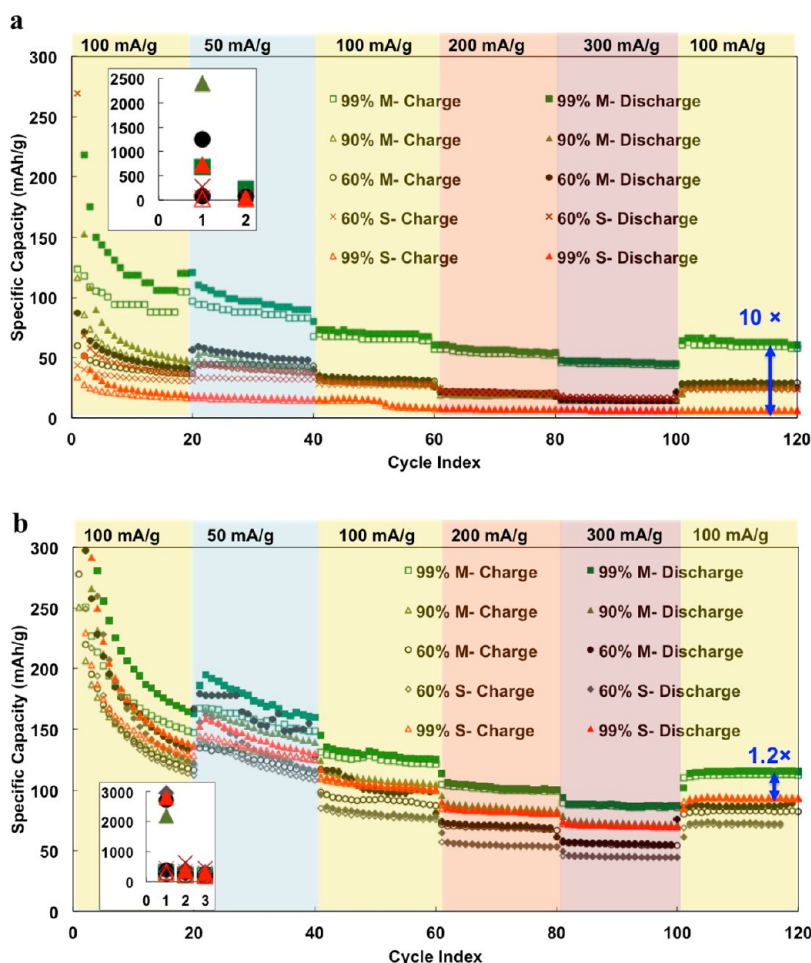
Figure 2. (a) Specific capacity of the vacuum-filtered SWCNT films without any post-treatment. In this case, the 99% metallic SWCNT films have 10 times higher lithium capacity than the 99% semiconducting SWCNT films. (b) Specific capacity of the nitric acid treated SWCNT films. Following acid treatment, the 99% metallic SWCNT films have 1.2 times higher lithium capacity than the 99% semiconducting SWCNT films. The insets show the early cycle capacity degradation characteristics.

Lithium ion battery half-cells were fabricated with 99%, 90%, 60%, 40%, and 1% purity metallic SWCNT films as the cathode and lithium foil as the anode with 1 M lithium hexafluorophosphate in ethylene carbonate—dimethyl carbonate (1:1) as the electrolyte. The open-circuit voltages of these cells were 2—3 V. The cells were galvanostatically charged/discharged between 0.02 and 2 V. The voltage—capacity curves of the first two cycles (Figure S1) possess two plateaus between 0.8 and 1.8 V in the first discharge cycle, indicating solid electrolyte interphase (SEI) formation. Figure 2a shows the specific capacity of these films, revealing that the 99% metallic SWCNT film has 10 times higher capacity than the 99% semiconducting (i.e., 1% metallic) SWCNT film.

It is important to note the effect of residual ionic surfactant here, which prevents full densification of the SWCNT film in addition to presenting irreversible reaction pathways for lithium (e.g., forming lithium dodecyl sulfate). To remove the residual surfactant, the SWCNT films were submerged in nitric acid (70%) for 18 h, rinsed in deionized water, and dried at 110 °C.

Figure 2b shows the lithium ion capacity for the resulting nitric acid treated films. The capacity of the metallic SWCNTs is increased by approximately 40%, while the lithium capacity for the semiconducting SWCNT is increased by more than 1000%. Consequently, the 99% metallic SWCNT film has only 20% higher capacity than the 99% semiconducting SWCNT film following surfactant removal and SWCNT film densification with nitric acid. The capacity of the mixed metallic and semiconducting films (i.e., 60% metallic and 60% semiconducting) is comparable to other SWCNT anodes[14,43] that have been tested with similar electrolytes, cell geometries, and applied rates, although pure semiconducting and pure metallic SWCNT films show improved capacity and cyclability. However, as mentioned before, the advantage of using carbon nanotubes in comparison with other additives or conventional graphite powders is not their capacity but rather their superior physical and mechanical properties that enable high-power applications and longer battery life.[44]

The nitric acid treated, 99% metallic SWCNT film was lithiated and delithiated for 500 cycles, showing a

a

b

c
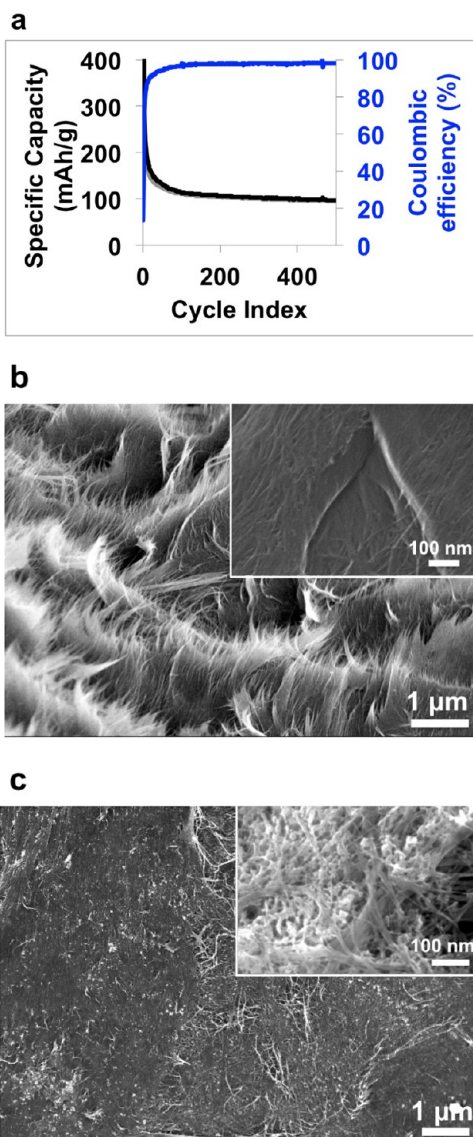
Figure 3. (a) Cycling performance of an acid-treated 99% metallic SWCNT film, showing stability after 500 cycles and a Coulombic efficiency of 98%. (b) SEM image of the freestanding, acid-treated, metallic SWCNT film before cycling. (c) SEM image of the freestanding, acid-treated, metallic SWCNT film following 100 charge/discharge cycles.

Coulombic efficiency of more than 98% (Figure 3a). The scanning electron microscopy (SEM) image of the prelithiated film is shown in Figure 3b. Figure 3c shows the SEM image of this film after 100 charge/discharge cycles, indicating the SEI that forms on the SWCNT bundles. This figure demonstrates that the freestanding SWCNT film is robust and the SWCNT network remains intact following significant charging and discharging.

Structural defects in carbon nanomaterials are known to increase the lithiation capacity.[45,46] However, in this case, the increase in capacity after acid treatment is not associated with increasing nanotube defect density. In particular, while more intensive acid treatment processes such as sonication in acid, acid

reflux at higher temperatures ($\sim$70 °C), and use of acid mixtures have been known to cause defects such as vacancies and holes in the nanotube structure,[46,47] the mild nitric acid treatment that was applied here is not expected to damage the nanotube structure. To verify this point, Raman spectroscopy was performed on 99% metallic, 65% semiconducting, and 99% semiconducting SWCNT films before and after acid treatment (Figure 4). The Raman peak at $\sim$1350 cm^{-1} is called the disorder-induced D-mode and corresponds to the SWCNT ends and sidewall defects.[48] The D peak intensity did not increase following the 18 h nitric acid treatment, indicating that the acid treatment does not lead to significant defect formation in the nanotube network.

Another potential effect of acid treatment on SWCNTs is doping. Nitric acid can cause formation of carboxyl, carbonyl, and amine functional groups on SWCNTs that are associated with a blue shift of the G band in the Raman spectra. This shift can also be observed by functionalization caused by ionic surfactants.[49] Figure 4b shows that the blue shift in the G band exists for surfactant-containing SWCNT films. However, when the surfactants are removed following the acid treatment, the G band is red-shifted to lower frequencies (Figure 4d). This result also indicates that the acid treatment is not leaving many functional groups on the SWCNTs that would enhance the blue shift in the G band and/or the water rinsing after acid treatment is removing most of the functional groups from the SWCNT network. The G$^-$ ($\sim$1550 cm^{-1}) and G$^+$ ($\sim$1590 cm^{-1}) peaks can also be used to characterize metallic and semiconducting SWCNTs.[50] In the 99% metallic film, the G$^-$ shoulder at $\sim$1550 cm^{-1} is broadened in comparison with the 99% semiconducting film. However, the difference is subtle here, since the films are $\sim$1 μm thick as opposed to the thin films or colloidal suspensions where electronic type differences are more apparent with Raman spectroscopy. Furthermore, it should be noted that at the 514 nm excitation wavelength the Raman signal is dominated by the semiconducting SWCNTs,[51] which is why the G bands for the 65% and 99% semiconducting films look similar.

X-ray photoelectron spectroscopy (XPS) characterization of the SWCNT films did not indicate a nitrogen peak, which also confirms that amine groups were removed by the rinsing process after acid treatment (Figure 5a). The high-resolution XPS scans of the carbon 1s and oxygen 1s peaks are shown in Figure S2. The oxygen 1s peak shows an intensity decrease after acid treatment, which is due to the removal of ionic surfactants that contain carboxyl and carbonyl groups. The Gaussian−Lorentzian deconvolution of the carbon 1s peak indicates C−C, C=O, and C−OH bonds both before and after nitric acid treatment.
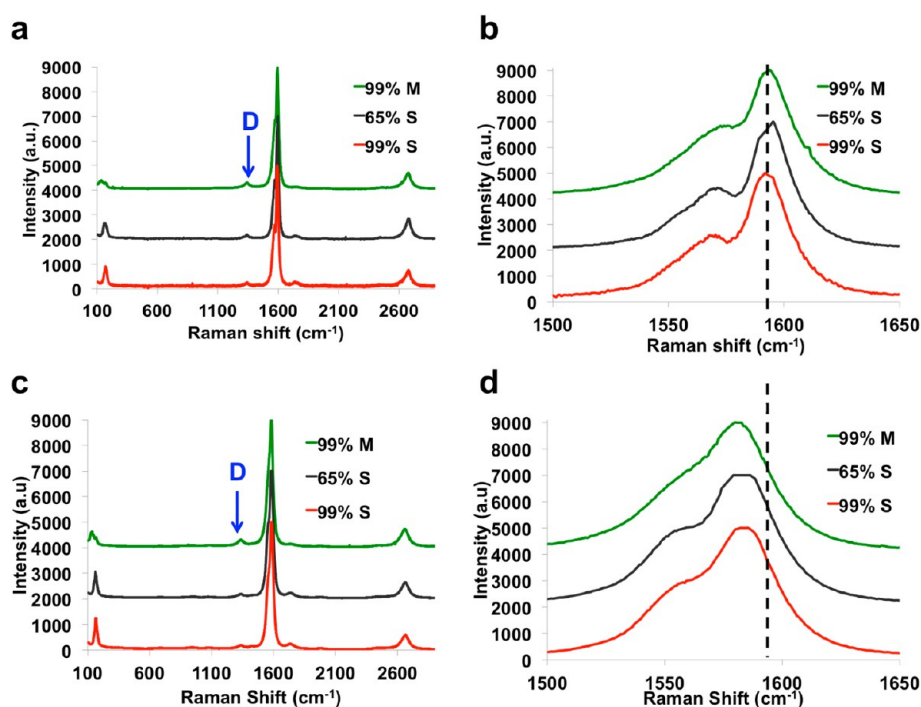
Figure 4. Raman spectra of 99% metallic, 65% semiconducting, and 99% semiconducting SWCNT films (a, b) before acid treatment and (c, d) after 18 h nitric acid treatment, showing no increase in the defect peak (D ≈ 1350 cm^{-1}) intensity as a result of the acid treatment. The spectra were normalized based on the G band (~1590 cm^{-1}) intensity. The G band is red-shifted by approximately 10 cm^{-1} after the acid treatment (b, d). The Raman excitation laser wavelength is 514 nm.
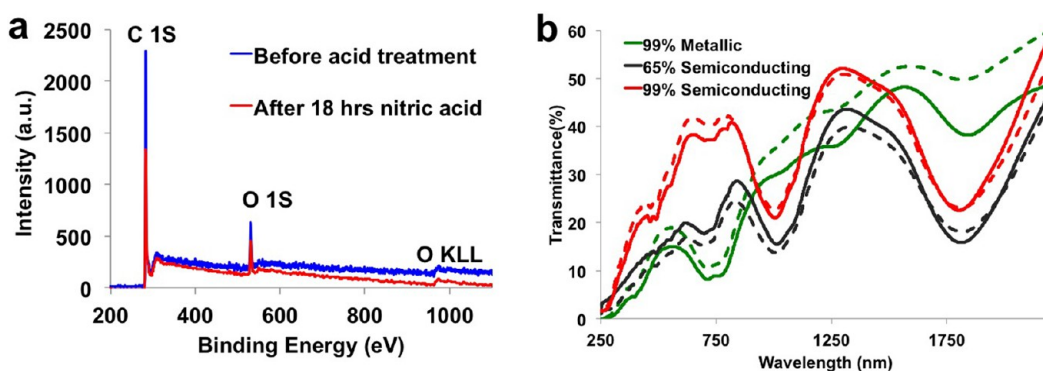

Figure 5. (a) X-ray photoelectron spectroscopy of the SWCNT network before acid treatment and after 18 h nitric acid treatment. (b) Optical transmittance spectra of the sorted SWCNT films before acid treatment (solid line) and after 18 h nitric acid treatment (dashed line).

Doping of the sorted SWCNT films with nitric acid can also result in bleaching of the corresponding metallic (M11 and M22) and semiconducting (S22 and S33) optical transition peaks.[52] We observed this bleaching by a color change that occurred in the sorted SWCNT films when they were immersed in acid (from green and red to gray for metallic and semiconducting SWCNT films, respectively). However, when the films were thoroughly rinsed in DI water, their color gradually returned to the initial condition. Figure 5b shows the optical transmittance spectra of the sorted SWCNT films before acid treatment and after acid treatment and DI water rinsing, indicating that the

optical transition peaks are restored after rinsing with DI water.

The sheet resistance of the freestanding SWCNT films was also measured, and no correlation between the sheet resistance of the sorted SWCNT films and their metallic or semiconducting content was observed since the freestanding SWCNT films are all beyond the percolation threshold.[53] Based on percolation theory, the conductivity of a SWCNT film is determined by the number of nanotubes contributing to the percolating network (film thickness) and the SWCNT–SWCNT junction resistance.[54] The junction resistance is much lower for metallic–metallic and semiconducting–semiconducting
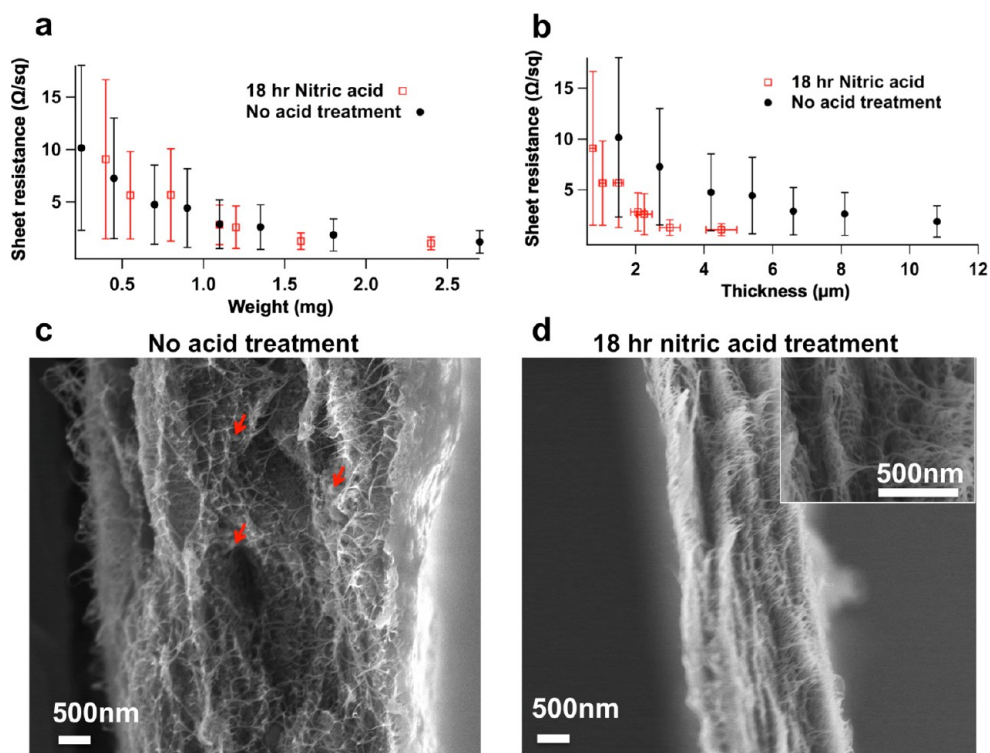
Figure 6. Effect of acid treatment on a 66% metallic (33% semiconducting) SWCNT film (error bars indicate sample-to-sample variations). (a) Sheet resistance *versus* film weight. (b) Sheet resistance *versus* film thickness. (c) Cross-sectional SEM image of the SWCNT film before acid treatment. Arrows indicate residual surfactants and other impurities in the SWCNT film. (d) Cross-sectional SEM image of the same SWCNT film after 18 h of nitric acid treatment.

SWCNT junctions in comparison with metallic–semiconducting junctions.[55] Thus, the conductivity of the sorted SWCNT film is highly dominated by the SWCNT film thickness. Indeed, the sheet resistance was observed to decrease as the SWCNT film thickness and weight are increased, as shown in Figure 6a,b. Since the area of the films was kept constant, the film thickness had a direct relationship with the film weight.

Nitric acid treatment is known to remove the residual ionic surfactant and impurities from the nanotube network and consume defective nanotubes.[52,56,57] The films were weighed before and after acid treatment, and a weight reduction of 15–20% was observed after the acid treatment, which was not dependent on the electronic type of the nanotubes. Within the sample-to-sample variation range, the nitric acid treatment did not have any effect on the weight-normalized sheet resistance of the SWCNT film. However, the nitric acid treatment causes 20–30% densification of the SWCNT film, and the thickness-normalized sheet resistance decreases as a result of nitric acid treatment (Figure 6b), which is consistent with the expected significant surfactant removal following nitric acid exposure.[56,57] The densification effect of the acid treatment is evident in the cross-sectional SEM images in Figure 6c,d. The SEM cross-section of the SWCNT film before acid treatment shows ionic surfactants and other impurities around the SWCNT bundles, which are absent after nitric acid treatment. To further

understand the effect of densification on the lithiation capacity of SWCNT films, theoretical calculations were performed.

THEORETICAL CALCULATIONS AND DISCUSSION

To investigate the binding of lithium to metallic and semiconducting SWCNTs, a combination of *ab initio* molecular dynamics (AIMD) and density functional theory (DFT) calculations of the binding energies of Li as a function of Li coverage and SWCNT–SWCNT separation values was performed. Armchair (11,11) SWCNTs and zigzag (20,0) SWCNTs were used to represent the metallic and semiconducting SWCNT families, respectively.[58] These nanotubes have relatively large diameters (~1.5 nm) that match the arc discharge grown SWCNTs that were used in the Experimental Section. The initial structures were first relaxed using DFT, and then further relaxations were induced using AIMD calculations to explore other possible minima of the potential energy surface and to find the lowest energy configurations, which were then used in further DFT calculations. We considered Li adsorption on the outer surfaces of the SWCNTs only, as we do not expect significant changes in the capacity contribution from the inner surfaces of the tubes, given the morphologies of the SWCNT bundles (aspect ratio and orientation) and previous work that reported that the outer surface is more favorable energetically.[30]
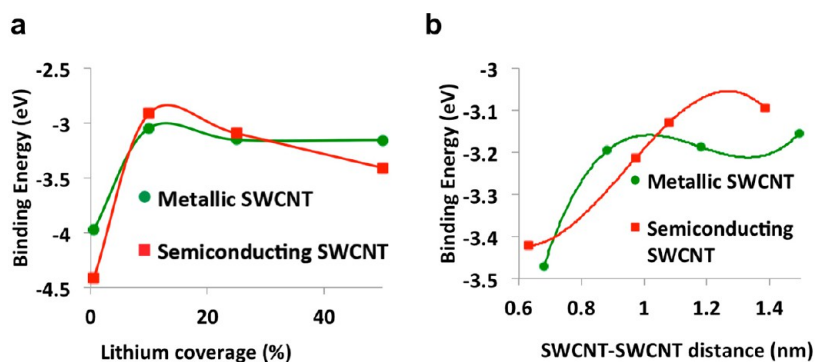
Figure 7. Calculated binding energy of lithium to a metallic SWCNT *versus* a semiconducting SWCNT as a function of (a) lithium coverage and (b) SWCNT−SWCNT separation distance at 25% lithium coverage.
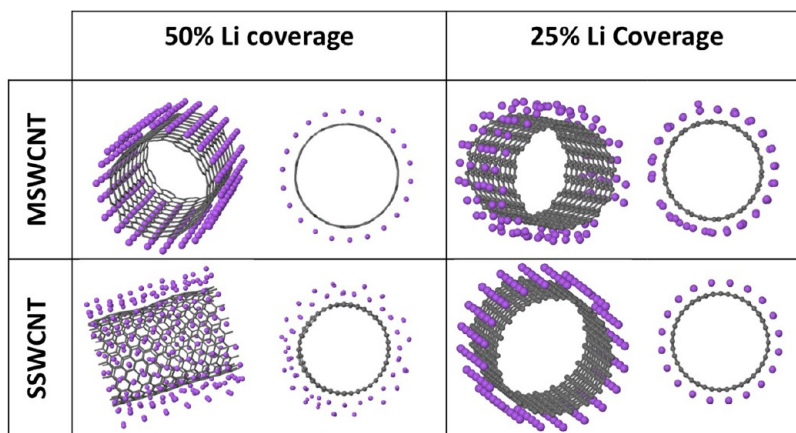

Figure 8. Lithium binding configurations on a metallic SWCNT (top) and a semiconducting SWCNT (bottom) at 50% and 25% lithium coverage.

The binding energies per Li (BEs) were calculated using the following expression: $BE(n) = (1/n)(E^{LiCNT} - E^{CNT} - nE_{Li})$, where E_n^{LiCNT} and E_n^{CNT} are the total energies of the SWCNT with and without lithium adsorbed on the surface, respectively. E_{Li} is the calculated total energy of bulk lithium per atom (1.9 eV), and n is the number of lithium atoms in the supercell. Both metallic and semiconducting SWCNTs exhibit (Figure 7a) a strong BE dependence as a function of Li coverage in the dilute coverage limit before leveling off at higher lithium coverage (>25%). The BE of the semiconducting SWCNT is higher (−4.41 eV) than the BE of the metallic SWCNT (−3.97 eV) at the dilute coverage limit, but reverses in favor of the metallic SWCNT for lithium coverage higher than 5%. The higher BE of a single lithium (*i.e.*, dilute limit) on the semiconducting SWCNT compared to the metallic SWCNT is due to a larger charge transfer from lithium to the nanotube in the case of the semiconducting SWCNT, while only a small charge polarization is observed for lithium interacting with the metallic SWCNT, as revealed by charge density difference plots (Figure S3).

At relatively higher lithium coverage, the increase in the Li−Li repulsion on the semiconducting SWCNT

begins to balance out the gain from the strong ionic-type binding with the nanotube surface (lithium on a semiconducting SWCNT is positively charged after donating charge to the nanotube). The second crossing is observed for lithium coverage higher than ~25%, again favoring a binding to the semiconducting SWCNT. The structure of the relaxed lithium layer (50% initial coverage) on the surface of the semiconducting SWCNT shows a bilayer configuration as opposed to the metallic SWCNT, which better accommodates the 50% lithium coverage maintaining the initial monolayer configuration (Figure 8). Again, Li−Li electrostatic repulsion on the semiconducting SWCNT limits the coverage of lithium on the surface.

To better understand the difference in binding between the monolayer and two-layer configurations, we investigated the binding of a lithium dimer in a flat configuration in which both lithium atoms adsorb to the nanotube surface (hollow sites), the upright configuration with one lithium binding to the surface and the second binding on top of the first lithium atom in the hollow site, and a case where both lithium atoms bind to the surface but are separated from each other. The results show that on the metallic SWCNT the flat Li−Li dimer configuration was 18 meV/Li lower in

energy than the separated configuration, while the upright configuration was higher (189 meV/Li) with a Li–Li bond length at 0.311 nm, which is a separation larger than the 0.304 nm of bulk Li, thus indicating a weaker Li–Li bond. On the semiconducting SWCNT, we could not stabilize the flat dimer configuration on the nanotube, as the Li–Li distance increased to 0.313 nm, giving a BE equal to the separated Li–Li configuration. The BE of the upright configuration, even though it was higher (173 meV/Li) than the separated configuration, resulted in a Li–Li bond length of 0.302 nm, indicating weaker bonding of lithium to the surface and, thus, favoring Li–Li bonding instead.

Indeed, at 50% lithium coverage, the actual amount of lithium binding directly to the nanotube surface is twice as large for the metallic SWCNT as it is for the semiconducting SWCNT. The larger binding energy of the semiconducting SWCNT at this high coverage compared to the metallic SWCNT is the result of increased interfacial energy between lithium and the nanotube in the metallic SWCNT case compared to the semiconducting SWCNT case, in which the bilayer configuration induces both a smaller energy penalty at the interface and a higher gain from increased Li–Li bonds. The presence of surfactants on the nanotube surfaces, which are present in the non-acid-treated samples, will have a much larger effect on the actual capacity of the semiconducting SWCNT, as the surfactants can hinder lithium from accessing the binding sites on the semiconducting SWCNT surface. This last observation could partially explain the jump in capacity improvement of the acid-treated semiconducting SWCNT, as now the amount of adsorbed surfactants on the surface is reduced.

However, 50% lithium uniform coverage (1 Li for 2 C atoms) is quite high and most likely unrealistic, and, as the bilayer lithium structure observed with the semiconducting SWCNT suggests, about 25% coverage seems to be the actual limit that can be accommodated by the surface. We do not expect to experimentally reach such high lithium coverage, even on the metallic SWCNTs, based on the experimental values reported so far for SWCNTs.[43] On the other hand, high values of Li coverage could be reached locally. Note that in the Li coverage range of interest (between 5% and 25%), metallic SWCNTs bind Li better than semiconducting SWCNTs, which is consistent with the

experimentally observed higher lithium capacity for the former.

Further calculations were performed at different nanotube–nanotube separations (*d*) at a fixed lithium coverage of 25% (Figure 7b). The results show a sharp increase in the binding energy for separations below 0.8 nm for the metallic SWCNTs, while the threshold of the binding energy change with nanotube–nanotube distance is about 1 nm for the semiconducting SWCNT, hence exhibiting higher sensitivity to the acid treatment. The AIMD calculations were performed with starting temperatures at 50, 100, and 300 K followed by DFT relaxations to explore other possible stable configurations, particularly at high coverage. The overall behavior remained practically unchanged for all coverage values except for 50% coverage (at $T = 300$ K only). In general, the threshold observed in the BE dependence on nanotube–nanotube separation, at which a sudden increase in BE is observed, is now less sharp, and the transition is more gradual. The BE difference between the metallic SWCNT and the semiconducting SWCNT at 50% is also reduced (from 0.25 eV/Li to 0.13 eV/Li). This reduction is due to the transfer of some of the Li from the first layer directly in contact with the SWCNT to the second Li layer, as well as some further nanotube shape relaxation. However, we believe that the structures obtained after AIMD at 50 and 100 K, which are similar, are more realistic as the overall SWCNT cylindrical shape is maintained.

CONCLUSIONS

In conclusion, we have studied the lithiation properties of monodisperse metallic and semiconducting SWCNTs using both experimental and theoretical techniques. Our study shows that metallic SWCNTs can better accommodate lithium, especially in the limit of large nanotube–nanotube spacing, resulting in an order of magnitude higher capacity in vacuum-filtered metallic SWCNT films compared to semiconducting SWCNTs. However, the lithiation of the semiconducting SWCNTs is found to be very sensitive to SWCNT–SWCNT distance, which implies that the lithiation capacity of semiconducting SWCNT films can be increased to levels comparable to metallic SWCNTs *via* a nitric acid treatment that causes SWCNT film densification. Overall, these results are likely to inform ongoing efforts to design SWCNT-based nanostructured membranes, templates, and additives in rechargeable lithium ion batteries.

MATERIALS AND METHODS

Preparation of the SWCNT Films. Electric arc discharge SWCNTs (P2, Carbon Solutions Inc.) were dispersed in an aqueous 1% w/v SC/SDS solution. They were then sorted by electronic type (metallic or semiconducting, depending on SC/SDS cosurfactant loading) *via* DGU in linear density gradients using iodixanol.[33,37] The centrifuge tubes were subsequently

fractionated, and the SWCNT electronic type purity was determined using optical absorbance spectra.[33] The solutions were dialyzed in 1% SC aqueous solution using Slide-A-Lyzer dialysis cassettes (20K MWCO, Pierce Protein Biology Products) to remove the iodixanol. The fractions were then combined to make solutions of the desired purities (purity was verified again using optical measurements) and were vacuum filtered through

Millipore mixed cellulose ester membranes (0.05 μm pore size, Millipore). A 50 mL amount of DI water was filtered over the SWCNT films to clean the residual surfactants. The films were then gently peeled off the membrane and dried on a hot plate at 110 °C.

Acid Treatment of the SWCNT Films. A 10 mL sample of nitric acid (70%) was poured into a beaker, and the freestanding SWCNT film was gently immersed for 18 h. Then, the acid was discarded from the beaker and exchanged with DI water several times. The DI water was changed two more times before the film was picked up with tweezers and moved to a fresh DI water bath. The film was then dried on a hot plate at 110 °C for a few minutes. Care was taken to ensure that the tweezers did not come into contact with the acid at any time in an effort to prevent contamination of the SWCNT film.

Film Characterization. After transferring the SWCNT film to a 300 nm SiO_2/Si substrate, the thickness of the films was measured by cross-sectional SEM after immersing the films in liquid nitrogen for a few minutes and cleaving the SiO_2/Si substrate. Optical transmittance curves were measured for each film *via* baseline-corrected UV−vis−NIR spectrophotometry (Cary 5000, Varian). Sheet resistance was measured using an in-line four-point probe and a Keithley 2400 sourcemeter. Raman spectra were measured using a 514 nm wavelength Ar/Kr mixed gas laser source.

Electrochemical Characterization. The SWCNT electrodes were tested in a coin cell geometry with the freestanding SWCNT films as cathodes and lithium metal as the anode. A solution of 1 M lithium hexafluorophosphate ($LiPF_6$) in anhydrous ethylene carbonate−dimethyl carbonate (1:1) was used as the electrolyte (Novolyte Technologies) with a trilayer polypropylene/polyethylene separator (Celgard, LLC). The coin cells were galvanostatically tested with a battery tester (Arbin Instruments).

Theoretical Calculations. The Kohn−Sham density functional method, as implemented in the Vienna *ab initio* simulation package (VASP),[59,60] was used with projected augmented wave potentials[61] and the generalized gradient approximation (GGA).[62] An energy cutoff of 420 eV was used. Gamma point sampling was used for the AIMD calculations at 50, 100, and 300 K to accelerate the structure relaxation. A microcanonical ensemble is simulated using the algorithm of Nosé.[63,64] The AIMD calculations were then followed by further spin-polarized DFT relaxation with Gamma $2 \times 2 \times 2$ K-point sampling. The binding energies were found to change by less than 5 meV/Li, when increasing the K-point grid to $3 \times 3 \times 3$. A single-point calculation using the tetrahedron method with Blöchl corrections was performed on the converged geometries. Large supercells were considered for both the (11,11) metallic SWCNT and the (20,0) semiconducting SWCNT with 220 and 240 carbon atoms for the metallic and semiconducting SWCNTs, respectively. The cells used in this study ranged between the two following sizes: (1) $30 \times 30 \times 12.21$ nm cells, representing parallel infinite length nanotubes with 1.5 nm diameter and 1.5 nm SWCNT−SWCNT spacing; (2) $22 \times 22 \times 12.21$ nm cells for ∼0.7 nm SWCNT−SWCNT spacing.

Conflict of Interest: The authors declare no competing financial interest.

Supporting Information Available: Voltage−capacity curves, XPS, and surface charge density plots. This material is available free of charge *via* the Internet at http://pubs.acs.org.

REFERENCES AND NOTES

1. Forney, M. W.; DiLeo, R. A.; Raisanen, A.; Ganter, M. J.; Staub, J. W.; Rogers, R. E.; Ridgley, R. D.; Landi, B. J. High Performance Silicon Free-Standing Anodes Fabricated by Low-Pressure and Plasma-Enhanced Chemical Vapor Deposition onto Carbon Nanotube Electrodes. *J. Power Sources* **2013**, *228*, 270–280.
2. Wu, Y.; Wei, Y.; Wang, J.; Jiang, K.; Fan, S. Conformal Fe_3O_4 Sheath on Aligned Carbon Nanotube Scaffolds as High-Performance Anodes for Lithium Ion Batteries. *Nano Lett.* **2013**, *13*, 818–823.
3. Shin, W. H.; Jeong, H. M.; Kim, B. G.; Kang, J. K.; Choi, J. W. Nitrogen-Doped Multiwall Carbon Nanotubes for Lithium Storage with Extremely High Capacity. *Nano Lett.* **2012**, *12*, 2283–2288.
4. Luo, S.; Wang, K.; Wang, J.; Jiang, K.; Li, Q.; Fan, S. Binder-Free $LiCoO_2$/Carbon Nanotube Cathodes for High-Performance Lithium Ion Batteries. *Adv. Mater.* **2012**, *24*, 2294–2298.
5. Jia, X.; Chen, Z.; Cui, X.; Peng, Y.; Wang, X.; Wang, G.; Wei, F.; Lu, Y. Building Robust Architectures of Carbon and Metal Oxide Nanocrystals toward High-Performance Anodes for Lithium-Ion Batteries. *ACS Nano* **2012**, *6*, 9911–9919.
6. Ko, S.; Lee, J.-I.; Yang, H. S.; Park, S.; Jeong, U. Mesoporous CuO Particles Threaded with CNTs for High-Performance Lithium-Ion Battery Anodes. *Adv. Mater.* **2012**, *24*, 4451–4456.
7. Xia, H.; Ragavendran, K. R.; Xie, J.; Lu, L. Ultrafine $LiMn_2O_4$/Carbon Nanotube Nanocomposite with Excellent Rate Capability and Cycling Stability for Lithium-Ion Batteries. *J. Power Sources* **2012**, *212*, 28–34.
8. Zhao, M.-Q.; Liu, X.-F.; Zhang, Q.; Tian, G.-L.; Huang, J.-Q.; Zhu, W.; Wei, F. Graphene/Single-Walled Carbon Nanotube Hybrids: One-Step Catalytic Growth and Applications for High-Rate Li-S Batteries. *ACS Nano* **2012**, *6*, 10759–10769.
9. Li, C.; Gu, L.; Tong, J.; Maier, J. Carbon Nanotube Wiring of Electrodes for High-Rate Lithium Batteries Using an Imidazolium-Based Ionic Liquid Precursor as Dispersant and Binder: A Case Study on Iron Fluoride Nanoparticles. *ACS Nano* **2011**, *5*, 2930–2938.
10. Goyal, A.; Reddy, A. L. M.; Ajayan, P. M. Flexible Carbon Nanotube-Cu_2O Hybrid Electrodes for Li-Ion Batteries. *Small* **2011**, *7*, 1709–1713.
11. Guo, J.; Xu, Y.; Wang, C. Sulfur-Impregnated Disordered Carbon Nanotubes Cathode for Lithium-Sulfur Batteries. *Nano Lett.* **2011**, *11*, 4288–4294.
12. Guo, B.; Wang, X.; Fulvio, P. F.; Chi, M.; Mahurin, S. M.; Sun, X.-G.; Dai, S. Soft-Templated Mesoporous Carbon-Carbon Nanotube Composites for High Performance Lithium-Ion Batteries. *Adv. Mater.* **2011**, *23*, 4661–4666.
13. Lee, S. W.; Yabuuchi, N.; Gallant, B. M.; Chen, S.; Kim, B.-S.; Hammond, P. T.; Shao-Horn, Y. High-Power Lithium Batteries from Functionalized Carbon-Nanotube Electrodes. *Nat. Nanotechnol.* **2010**, *5*, 531–537.
14. DiLeo, R. A.; Castiglia, A.; Ganter, M. J.; Rogers, R. E.; Cress, C. D.; Raffaelle, R. P.; Landi, B. J. Enhanced Capacity and Rate Capability of Carbon Nanotube Based Anodes with Titanium Contacts for Lithium Ion Batteries. *ACS Nano* **2010**, *4*, 6121–6131.
15. Frackowiak, E. Electrochemical Storage of Energy in Carbon Nanotubes and Nanostructured Carbons. *Carbon* **2002**, *40*, 1775–1787.
16. Ng, S.; Wang, J.; Guo, Z.; Chen, J.; Wang, G.; Liu, H. Single Wall Carbon Nanotube Paper as Anode for Lithium-Ion Battery. *Electrochim. Acta* **2005**, *51*, 23–28.
17. Wang, W.; Kumta, P. N. Nanostructured Hybrid Silicon/Carbon Nanotube Heterostructures: Reversible High-Capacity Lithium-Ion Anodes. *ACS Nano* **2010**, *4*, 2233–2241.
18. Chou, S.-L.; Zhao, Y.; Wang, J.-Z.; Chen, Z.-X.; Liu, H.-K.; Dou, S.-X. Silicon/Single-Walled Carbon Nanotube Composite Paper as a Flexible Anode Material for Lithium Ion Batteries. *J. Phys. Chem. C* **2010**, *114*, 15862–15867.

19. Ren, J.; Yang, J.; Abouimrane, A.; Wang, D.; Amine, K. SnO$_2$ Nanocrystals Deposited on Multiwalled Carbon Nanotubes with Superior Stability as Anode Material for Li-Ion Batteries. *J. Power Sources* **2011**, *196*, 8701–8705.

20. Noerochim, L.; Wang, J.-Z.; Chou, S.-L.; Wexler, D.; Liu, H.-K. Free-Standing Single-Walled Carbon Nanotube/ SnO$_2$ Anode Paper for Flexible Lithium-Ion Batteries. *Carbon* **2012**, *50*, 1289–1297.

21. Chou, S.-L.; Wang, J.-Z.; Chen, Z.-X.; Liu, H.-K.; Dou, S.-X. Hollow Hematite Nanosphere/Carbon Nanotube Composite: Mass Production and Its High-Rate Lithium Storage Properties. *Nanotechnology* **2011**, *22*, 265401.

22. Huang, J.; Jiang, Z. The Preparation and Characterization of Li$_4$Ti$_5$O$_{12}$/Carbon Nano-Tubes for Lithium Ion Battery. *Electrochim. Acta* **2008**, *53*, 7756–7759.

23. Riley, L. A.; Cavanagh, A. S.; George, S. M.; Jung, Y. S.; Yan, Y.; Lee, S.-H.; Dillon, A. C. Conformal Surface Coatings to Enable High Volume Expansion Li-Ion Anode Materials. *ChemPhysChem* **2010**, *11*, 2124–2130.

24. Wu, H.; Yu, G.; Pan, L.; Liu, N.; McDowell, M. T.; Bao, Z.; Cui, Y. Stable Li-Ion Battery Anodes by in-Situ Polymerization of Conducting Hydrogel to Conformally Coat Silicon Nanoparticles. *Nat. Commun.* **2013**, *4*, 1943.

25. Wang, K.; Luo, S.; Wu, Y.; He, X.; Zhao, F.; Wang, J.; Jiang, K.; Fan, S. Super-Aligned Carbon Nanotube Films as Current Collectors for Lightweight and Flexible Lithium Ion Batteries. *Adv. Funct. Mater.* **2013**, *23*, 846–853.

26. Kim, H.; Lee, J. T.; Yushin, G. High Temperature Stabilization of Lithium−Sulfur Cells with Carbon Nanotube Current Collector. *J. Power Sources* **2013**, *226*, 256–265.

27. Hersam, M. C. Progress towards Monodisperse Single-Walled Carbon Nanotubes. *Nat. Nanotechnol.* **2008**, *3*, 387–394.

28. Liu, J.; Hersam, M. C. Recent Developments in Carbon Nanotube Sorting and Selective Growth. *MRS Bull.* **2010**, *35*, 270–280.

29. Garau, C. Lithium Diffusion in Single-Walled Carbon Nanotubes: A Theoretical Study. *Chem. Phys. Lett.* **2003**, *374*, 548–555.

30. Kar, T.; Pattanayak, J.; Scheiner, S. Insertion of Lithium Ions into Carbon Nanotubes: An ab Initio Study. *J. Phys. Chem. A* **2001**, *105*, 10397–10403.

31. Song, B.; Yang, J.; Zhao, J.; Fang, H. Intercalation and Diffusion of Lithium Ions in a Carbon Nanotube Bundle by ab Initio Molecular Dynamics Simulations. *Energy Environ. Sci.* **2011**, *4*, 1379.

32. Kawasaki, S.; Hara, T.; Iwai, Y.; Suzuki, Y. Metallic and Semiconducting Single-Walled Carbon Nanotubes as the Anode Material of Li Ion Secondary Battery. *Mater. Lett.* **2008**, *62*, 2917–2920.

33. Green, A. A.; Hersam, M. C. Colored Semitransparent Conductive Coatings Consisting of Monodisperse Metallic Single-Walled Carbon Nanotubes. *Nano Lett.* **2008**, *8*, 1417–1422.

34. Wang, B.; Poa, C. H. P.; Wei, L.; Li, L.-J.; Yang, Y.; Chen, Y. (n,m) Selectivity of Single-Walled Carbon Nanotubes by Different Carbon Precursors on Co-Mo Catalysts. *J. Am. Chem. Soc.* **2007**, *129*, 9014–9019.

35. Wang, Y.; Liu, Y.; Li, X.; Cao, L.; Wei, D.; Zhang, H.; Shi, D.; Yu, G.; Kajiura, H.; Li, Y. Direct Enrichment of Metallic Single-Walled Carbon Nanotubes Induced by the Different Molecular Composition of Monohydroxy Alcohol Homologues. *Small* **2007**, *3*, 1486–1490.

36. Liu, H.; Nishide, D.; Tanaka, T.; Kataura, H. Large-Scale Single-Chirality Separation of Single-Wall Carbon Nanotubes by Simple Gel Chromatography. *Nat. Commun.* **2011**, *2*, 309.

37. Arnold, M. S.; Green, A. a; Hulvat, J. F.; Stupp, S. I.; Hersam, M. C. Sorting Carbon Nanotubes by Electronic Structure Using Density Differentiation. *Nat. Nanotechnol.* **2006**, *1*, 60–65.

38. Jin, S. H.; Dunham, S. N.; Song, J.; Xie, X.; Kim, J.; Lu, C.; Islam, A.; Du, F.; Kim, J.; Felts, J.; *et al.* Using Nanoscale Thermocapillary Flows to Create Arrays of Purely Semiconducting Single-Walled Carbon Nanotubes. *Nat. Nanotechnol.* **2013**, 1–9.

39. Green, A. A.; Duch, M. C.; Hersam, M. C. Isolation of Single-Walled Carbon Nanotube Enantiomers by Density Differentiation. *Nano Res.* **2010**, *2*, 69–77.

40. Antaris, A. L.; Seo, J.-W. T.; Green, A. A; Hersam, M. C. Sorting Single-Walled Carbon Nanotubes by Electronic Type Using Nonionic, Biocompatible Block Copolymers. *ACS Nano* **2010**, *4*, 4725–4732.

41. Green, A. A.; Hersam, M. C. Ultracentrifugation of Single-Walled Nanotubes. *Mater. Today* **2007**, *10*, 59–60.

42. Smith, R. J.; King, P. J.; Lotya, M.; Wirtz, C.; Khan, U.; De, S.; O'Neill, A.; Duesberg, G. S.; Grunlan, J. C.; Moriarty; *et al.* Large-Scale Exfoliation of Inorganic Layered Compounds in Aqueous Surfactant Solutions. *Adv. Mater.* **2011**, *23*, 3944–3948.

43. Landi, B. J.; Ganter, M. J.; Schauerman, C. M.; Cress, C. D.; Raffaelle, R. P. Lithium Ion Capacity of Single Wall Carbon Nanotube Paper Electrodes. *J. Phys. Chem. C* **2008**, *112*, 7509–7515.

44. Landi, B. J.; Ganter, M. J.; Cress, C. D.; DiLeo, R. A.; Raffaelle, R. P. Carbon Nanotubes for Lithium Ion Batteries. *Energy Environ. Sci.* **2009**, *2*, 638–654.

45. Zhao, X.; Hayner, C. M.; Kung, M. C.; Kung, H. H. In-Plane Vacancy-Enabled High-Power Si-Graphene Composite Electrode for Lithium-Ion Batteries. *Adv. Energy Mater.* **2011**, *1*, 1079–1084.

46. Eom, J. Y.; Kwon, H. S.; Liu, J.; Zhou, O. Lithium Insertion into Purified and Etched Multi-Walled Carbon Nanotubes Synthesized on Supported Catalysts by Thermal CVD. *Carbon* **2004**, *42*, 2589–2596.

47. Yang, J.; Wang, S.; Zhou, X.; Xie, J. Electrochemical Behaviors of Functionalized Carbon Nanotubes in LiPF$_6$/ EC+DMC Electrolyte. *Int. J. Electrochem. Sci.* **2012**, *7*, 6118–6126.

48. Hennrich, F.; Krupke, R.; Lebedkin, S.; Arnold, K.; Fischer, R.; Resasco, D. E.; Kappes, M. M. Raman Spectroscopy of Individual Single-Walled Carbon Nanotubes from Various Sources. *J. Phys. Chem. B* **2005**, *109*, 10567–10573.

49. Park, Y. T.; Ham, A. Y.; Grunlan, J. C. Heating and Acid Doping Thin Film Carbon Nanotube Assemblies for High Transparency and Low Sheet Resistance. *J. Mater. Chem.* **2011**, *21*, 363–368.

50. Dresselhaus, M. S.; Dresselhaus, G.; Jorio, A.; Filho, A. G. S.; Saito, R. Raman Spectroscopy on Isolated Single Wall Carbon Nanotubes. *Carbon* **2002**, *40*, 2043–2061.

51. Huang, H.; Maruyama, R.; Noda, K.; Kajiura, H.; Kadono, K. Preferential Destruction of Metallic Single-Walled Carbon Nanotubes by Laser Irradiation. *J. Phys. Chem. B* **2006**, *110*, 7316–7320.

52. Tyler, T. P.; Brock, R. E.; Karmel, H. J.; Marks, T. J.; Hersam, M. C. Electronically Monodisperse Single-Walled Carbon Nanotube Thin Films as Transparent Conducting Anodes in Organic Photovoltaic Devices. *Adv. Energy Mater.* **2011**, *1*, 785–791.

53. Cao, Q.; Rogers, J. A. Ultrathin Films of Single-Walled Carbon Nanotubes for Electronics and Sensors: A Review of Fundamental and Applied Aspects. *Adv. Mater.* **2009**, *21*, 29–53.

54. Hu, L.; Hecht, D. S.; Gruner, G. Percolation in Transparent and Conducting Carbon Nanotube Networks. *Nano Lett.* **2004**, *4*, 2513–2517.

55. Fuhrer, M. S. Crossed Nanotube Junctions. *Science* **2000**, *288*, 494–497.

56. Ng, M. H. A.; Hartadi, L. T.; Tan, H.; Poa, C. H. P. Efficient Coating of Transparent and Conductive Carbon Nanotube Thin Films on Plastic Substrates. *Nanotechnology* **2008**, *19*, 205703–205708.

57. Gao, J.; Wang, W. Y.; Cui, L. J.; Chen, L. T.; Hu, X. Y.; Li, H.; Geng, H. Z. Effect of Different Concentrations of Nitric Acid on the Conductivity of Single-Walled Carbon Nanotube Transparent Films. *Adv. Mater. Res.* **2013**, *658*, 3–7.

58. Dresselhaus, M. S.; Dresselhaus, G.; Eklund, P. C.; Rao, A. M. In *The Physics of Fullerene-Based and Fullerene-Related Materials*; Anderoni, W., Ed.; Springer: The Netherlands, 2000; pp 331−379.

59. Kresse, G.; Hafner, J. Ab Initio Molecular Dynamics for Liquid Metals. *Phys. Rev. B* **1993**, *47*, 558–561.

60. Kresse, G.; Furthmüller, J. Efficient Iterative Schemes for ab Initio Total-Energy Calculations Using a Plane-Wave Basis Set. *Phys. Rev. B, Condens. Matter* **1996**, *54*, 11169–11186.

61. Blöchl, P. E. Projector Augmented-Wave Method. *Phys. Rev. B* **1994**, *50*, 17953–17979.

62. Perdew, J. P.; Wang, Y. Accurate and Simple Analytic Representation of the Electron-Gas Correlation Energy. *Phys. Rev. B* **1992**, *45*, 13244–13249.

63. Nosé, S. A Unified Formulation of the Constant Temperature Molecular Dynamics Methods. *J. Chem. Phys.* **1984**, *81*, 511–519.

64. Nosé, S. Constant Temperature Molecular Dynamics Methods. *Prog. Theor. Phys. Suppl.* **1991**, *103*, 1–46.